universe

MDPI

Article

Ordinary Muon Capture on ^{136}Ba: Comparative Study Using the Shell Model and pnQRPA

Patricia Gimeno [1,*], Lotta Jokiniemi [2], Jenni Kotila [1,3,4], Marlom Ramalho [1] and Jouni Suhonen [1]

[1] Department of Physics, University of Jyväskylä, P.O. Box 35 (YFL), 40014 Jyväskylä, Finland; jenni.kotila@jyu.fi (J.K.); madeoliv@jyu.fi (M.R.); jouni.t.suhonen@jyu.fi (J.S.)
[2] TRIUMF, 4004 Wesbrook Mall, Vancouver, BC V6T 2A3, Canada; ljokiniemi@triumf.ca
[3] Finnish Institute for Educational Research, University of Jyväskylä, P.O. Box 35 (YFL), 40014 Jyväskylä, Finland
[4] Center for Theoretical Physics, Sloane Physics Laboratory, Yale University, New Haven, CT 06520-8120, USA
* Correspondence: patricia.p.gimenoestivill@student.jyu.fi

Abstract: In this work, we present a study of ordinary muon capture (OMC) on ^{136}Ba, the daughter nucleus of ^{136}Xe double beta decay (DBD). The OMC rates at low-lying nuclear states (below 1 MeV of excitation energy) in ^{136}Cs are assessed by using both the interacting shell model (ISM) and proton–neutron quasiparticle random-phase approximation (pnQRPA). We also add chiral two-body (2BC) meson-exchange currents and use an exact Dirac wave function for the captured s-orbital muon. OMC can be viewed as a complementary probe of the wave functions in ^{136}Cs, the intermediate nucleus of the ^{136}Xe DBD. At the same time, OMC can be considered a powerful probe of the effective values of weak axial-type couplings in a 100 MeV momentum exchange region, which is relevant for neutrinoless DBD. The present work represents the first attempt to compare the ISM and pnQRPA results for OMC on a heavy nucleus while also including the exact muon wave function and the 2BC. The sensitivity estimates of the current and future neutrinoless DBD experiments will clearly benefit from future OMC measurements taken using OMC calculations similar to the one presented here.

Keywords: neutrino physics; muon capture rates; double beta decays; weak interaction

Citation: Gimeno, P. ; Jokiniemi, L.; Kotila, J.; Ramalho, M.; Suhonen, J. Ordinary Muon Capture on ^{136}Ba: Comparative Study Using the Shell Model and pnQRPA. *Universe* **2023**, *9*, 270. https://doi.org/10.3390/universe9060270

Academic Editors: Mihai Horoi and Andrei Neacsu

Received: 24 April 2023
Revised: 31 May 2023
Accepted: 2 June 2023
Published: 5 June 2023

1. Introduction

Neutrinoless double beta decay (NDBD) has been one of the key issues in nuclear and particle physics for many decades [1–4]. A number of experiments have tried to measure this hypothetical process [5], and numerous nuclear structure calculations have tried or are trying to address the associated nuclear matrix elements (NME) (for a comprehensive list, see References [1,4,5]). In particular, several efforts have been made to compute these NME in the interacting shell model (ISM) (see, e.g., References [6–9]) and proton–neutron quasiparticle random-phase approximation (pnQRPA) (see, e.g., the reviews [5,10]). The theory estimates for NDBD are pestered by sizable discrepancies between the NME—which enter the NDBD rate in second power—obtained using different nuclear many-body methods [5]. Furthermore, there is additional uncertainty related to the possible need to quench the Gamow–Teller type of spin–isospin operator $\sigma\tau$, which dominates the NDBD NME. Since $g_{\rm A}$ multiplies this operator, the quenching of $\sigma\tau$ by a factor q can be interpreted also as quenching of $g_{\rm A}$ in terms of $g_{\rm A}^{\rm eff} = qg_{\rm A}^{\rm bare}$, where we take $g_{\rm A}^{\rm bare} = 1.27$ as the bare value of $g_{\rm A}$, obtained from the beta decay of a free neutron (there have been many measurements, see, e.g., Reference [11]). In ISM and pnQRPA studies, appropriate quenching in a low-momentum exchange regime can be found by adjusting the calculations to existing data on beta and two-neutrino double-beta decay [12–14]. However, the situation in higher momentum exchange is less clear [15]. The need for quenching is a result of deficiencies in the nuclear many-body methods used in the calculations and of the omission

of the two-body meson-exchange currents, as discussed exhaustively for light nuclei in Reference [16].

The above-mentioned work on the effective value of g_A concerns processes with momentum exchanges between the involved lepton(s) and the nucleus within the range of a few MeV[1]. Contrary to this, the momentum exchanges involved in the NDBD are of the order of 100 MeV. This means that one cannot use the obtained results for the quenching related to the meson-exchange currents directly for the NDBD, but one has to evolve those to higher momentum exchanges, as was first achieved in Reference [15] by implementing chiral two-body currents (2BC) in the Gamow–Teller type of transition. Recently, these two-body currents were implemented in the nuclear ordinary muon capture (OMC) formalism of Morita and Fujii [17] in Reference [18] for the light nucleus ^{24}Mg.

OMC (we refer the readers to Reference [19]) is able to probe nuclear wave functions within wide ranges of energies and spins of nuclear excitation, which is relevant for NDBD [20,21]. At the same time, OMC can be used to probe the effective values of both g_A and g_P—the induced pseudoscalar coupling—in a momentum exchange region typical for NDBD [22]. In addition, comparison of the muon capture and NDBD matrix elements shows clear correlations, as detailed in References [21,23].

As mentioned above, 2BCs were implemented in Reference [18] for OMC on ^{24}Mg. There, ISM results were compared with those of the ab initio method, the valence-space in-medium similarity renormalization group (VS-IMSRG). Here, we want to extend the ISM study to a heavy nucleus example, ^{136}Ba, the final nucleus of the ^{136}Xe NDBD. The nucleus ^{136}Xe is highly important in terms of NDBD measurements [24–27]. In the present work, we compare the ISM- and pnQRPA-computed partial OMC rates with each other and study the effects of the 2BC on them for final states below roughly 1 MeV of excitation energy in ^{136}Cs. This energy range is accessible to present state-of-the-art OMC experiments, such as that of the MONUMENT Collaboration [28].

OMC experiments have evolved from early measurements [29,30] towards larger-scale ones, as demonstrated by the MONUMENT experiments at PSI, Switzerland [28] and the OMC experiments at RCNP (the Research Center for Nuclear Physics) in Osaka, Japan [31–33]. For more details on the timeline of the RCNP experiments, see the recent review [34]. Undoubtedly, within the next few years we will have a wealth of new OMC data to be compared with theoretical results obtained using various nuclear models also found in the NDBD calculations.

2. Theoretical Framework

Ordinary muon capture (OMC)—as differentiated explicitly from its radiative counterpart—on the even–even nucleus ^{136}Ba populates the final states of the odd–odd nucleus ^{136}Cs according to the schematic

$$\mu^- + {}^{136}\mathrm{Ba}(0^+_{\mathrm{g.s.}}) \rightarrow \nu_\mu + {}^{136}\mathrm{Cs}(J^\pi_f)\,, \tag{1}$$

where a negative muon (μ^-) is captured by the ground state of ^{136}Ba, leading to the final states J^π_f in ^{136}Cs, where J is the angular momentum and π the parity. At the same time, a muon neutrino ν_μ is emitted.

2.1. Bound-Muon S-Orbital Wave Function

Here we compute the OMC rates by using the formalism of Morita and Fujii [17]. In this formalism, it is straightforward to implement the exact Dirac wave function of the muon, as described in detail in Reference [18]. The Dirac wave function can be written as

$$\psi_\mu(\kappa,\mu;\boldsymbol{r}) = \psi^{(\mu)}_{\kappa\mu} = \begin{bmatrix} -iF_\kappa(r)\chi_{-\kappa\mu}(\hat{r}) \\ G_\kappa(r)\chi_{\kappa\mu}(\hat{r}) \end{bmatrix}, \tag{2}$$

where G_κ and F_κ are the radial wave functions of the bound state [17] and $\chi_{\kappa\mu}$ are normalized spherical spinors. The index κ is related to the orbital quantum number l in the following manner

$$\begin{cases} l = \kappa \text{ and } j = l - \frac{1}{2} & \text{for } \kappa > 0 \\ l = -\kappa - 1 \text{ and } j = l + \frac{1}{2} & \text{for } \kappa < 0 \,. \end{cases} \tag{3}$$

After being stopped in the outer shells of an atom, the negative muon transits to the lowest atomic orbital, the $1s_{1/2}$ state, which corresponds to $\kappa = -1$ and $\mu = \pm 1/2$. The corresponding large and small components of the bound-muon wave function—G_{-1} and F_{-1}—from Equation (2) can be numerically solved from the Dirac wave equations in the Coulomb field created by the nucleus [18]. Here we assume a nucleus with a uniform spherical charge distribution with a charge radius $R_c = r_0 A^{1/3}$ and with $r_0 = 1.2$ fm and A being the nuclear mass number. The large component of the wave function accounts for a major part of the physics of the captured muon, while the small part accounts only for some 1% of the wave function, see, e.g., Figure 1 in Reference [18]. Hence, we can safely neglect the small part. The G_{-1} part can be compared with the Bethe–Salpeter (BS) equation [35] for a point nucleus:

$$G_{-1} = (2Z/a_0)^{\frac{3}{2}} \sqrt{\frac{1+\gamma}{2\Gamma(2\gamma+1)}} \left(\frac{2Zr}{a_0}\right)^{\gamma-1} e^{-Zr/a_0} \,. \tag{4}$$

Here, Z is the atomic number of the nucleus, $\gamma = \sqrt{1-(\alpha Z)^2}$, with the fine-structure constant α and the Bohr radius of the μ-mesonic atom

$$a_0 = \frac{1}{m'_\mu \alpha} \,. \tag{5}$$

Here we have defined the reduced muon mass as

$$m'_\mu = \frac{m_\mu}{1 + \frac{m_\mu}{AM}}, \tag{6}$$

where M is the (average) nucleon mass, and AM is the mass of the mother (and daughter) nucleus.

In Figure 1, we display the exact Dirac s-orbital wave function (large component) and its various degrees of approximation for ^{136}Ba. In the figure, it can be seen that the point–nucleus exact wave function and its BS approximation are quite close to each other, except at very short distances $r \lesssim 3$ fm. Contrary to this, the exact finite-nucleus Dirac wave function deviates considerably from the other two, especially within the nucleus (the gray band in the figure). This is a much more drastic effect than the corresponding one for a light nucleus, such as ^{24}Mg (see Figure 1 of [18]).

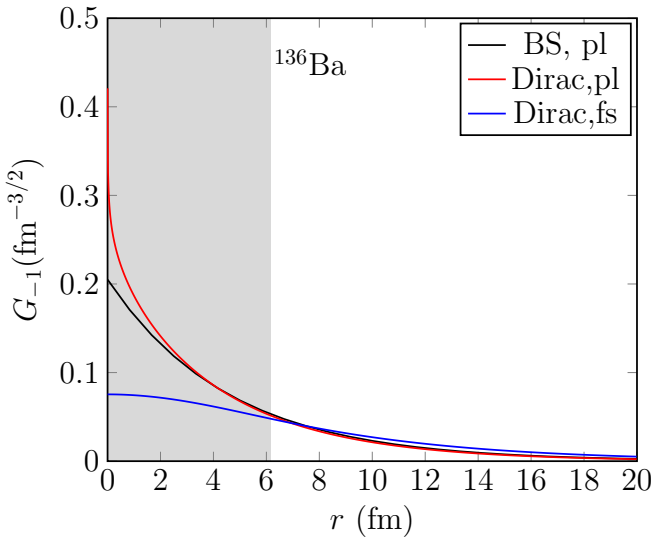

Figure 1. Comparison of the large component of the exact muon wave function for a finite nucleus with a uniform spherical charge distribution (blue line) with a corresponding one for a point-like nucleus (red line) and its Bethe–Salpeter (BS) approximation (black line). The gray band denotes the range inside the nucleus.

2.2. Muon-Capture Rates

Calculation of the OMC rates is achieved using the Morita–Fujii formalism [17] and its extension developed in Reference [36,37] in order to treat small OMC rates in a more reliable way. The OMC rate of the process (1) can be expressed as

$$W = 2P(2J_f + 1)\left(1 - \frac{q}{m_\mu + AM}\right)q^2 \,, \tag{7}$$

where the momentum exchange (q value) can be expressed as

$$q = (m_\mu - W_0)\left(1 - \frac{m_\mu}{2(m_\mu + AM)}\right) \,. \tag{8}$$

Here, J_f is the final-state spin-parity, M the average nucleon mass, and m_μ (m_e) is the rest mass of the muon (electron). The threshold energy $W_0 = M_f - M_i + m_e + E_X$ contains M_i and M_f as the masses of the initial and final nuclei and E_X the excitation energy of the final nuclear state in ^{136}Cs. The rate function P contains the nuclear matrix elements, phase–space factors, and combinations of the weak couplings g_A (axial–vector coupling), g_P (induced pseudoscalar coupling), and $g_\mathrm{M} = 1 + \mu_p - \mu_n$ (induced weak-magnetism coupling), where μ_p and μ_n are the anomalous magnetic moments of the proton and the neutron. In the present work, we use the Goldberger–Treiman partially conserved axial vector current (PCAC) value for the ratio of the two axial-type couplings:

$$g_P/g_A = \frac{2Mq}{q^2 + m_\pi^2} \approx 6.8 \,, \tag{9}$$

where $m_\pi = 138.04$ MeV is the pion rest mass. Unless otherwise indicated, we adopt the free-neutron value $g_\mathrm{A} = 1.27$ in our calculations. Explicit expressions for the rate function P, containing all of the next-to-leading-order terms, can be found in detail in Reference [37], and we do not repeat those expressions in this article. It should be noted that at low excitation energies, as considered in the present work, $W_0/m_\mu \ll 1$ and, hence, the nuclear matrix elements in P depend only weakly on the excitation energy E_X of the nuclear state.

2.3. Chiral Two-Body Currents

We take the effect of the 2BC into account by making the replacements

$$g_A \to (1 + \delta_a(q^2))g_A \tag{10}$$

and

$$g_P \to \left(1 - \frac{q^2 + m_\pi^2}{q^2}\delta_a^P(q^2)\right)g_P\,, \tag{11}$$

where the 2BC contributions $\delta_a(q^2)$ and $\delta_a^P(q^2)$ are approximated by the normal-ordered one-body part of the chiral two-body currents, as was achieved in Reference [38]. Normal ordering is conducted with respect to a Fermi gas reference state with density ρ. In the present work, we take the involved integrals in $\delta_a(q^2)$ and $\delta_a^P(q^2)$ to be those of [39] with the density range $\rho = 0.09$–0.11 fm^{-3}. We use the same values of the involved constants as in Reference [38], as does Reference [40]. For the low-energy constants (LEC) c_1, c_3, c_4, c_6, and c_D involved in the currents, we used the values listed in Table V of Reference [38]. The constant c_D was adjusted in Reference [38] so that the axial vector correction $\delta_a(q^2)$ corresponded to the typical 20–30% axial vector quenching (or $g_{\rm A}^{\rm eff} = 0.89$–$1.02$ in terms of an effective coupling) at $q = 0$ MeV: the pair ($\rho = 0.09$ fm^{-3}, $c_D = -6.08$) giving the most quenching and ($\rho = 0.11$ fm^{-3}, $c_D = 0.3$) the least. We use the ranges of $\delta a(q^2)$ and $\delta a^P(q^2)$ produced by these parameter choices for quantification of the uncertainties of our computed OMC rates. The corresponding 2BCs are displayed in Figure 2 where the relevant momentum exchange region is indicated by a vertical band. For the excitation energy region discussed in the present work, the momentum exchanges are contained within the interval $q_{\rm OMC} = 101.5$–102.6 MeV and the 2BC contributions within the intervals $\delta_a(q^2) = -(0.210$–$0.310)$ and $\delta_a^P(q^2) = 0.178$–0.180.

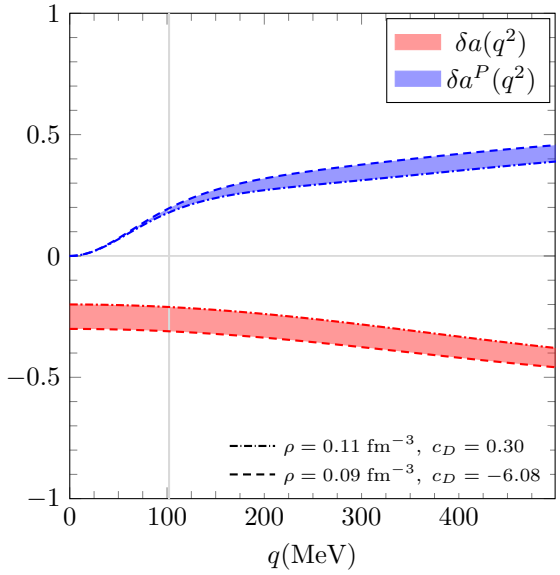

Figure 2. The two-body currents used in the present work are functions of momentum exchange. The dashed lines denote the currents obtained by $\rho = 0.09$ fm^{-3} and $c_D = -6.08$, and the dotted lines indicate those obtained with $\rho = 0.11$ fm^{-3} and $c_D = 0.30$. The typical momentum exchange region of the transitions considered in the present work is denoted by a vertical gray band.

The corrections coming from the inclusion of the 2BC at the relevant momentum exchange region correspond to a range $g_{\rm A}^{\rm eff}(q_{\rm OMC}) = 0.88$–$1.00$ of quenched values of the weak axial coupling and a range of $g_{\rm P}^{\rm eff}(q_{\rm OMC}) = 4.26$–$4.27$ of quenched values of the induced pseudoscalar coupling.

2.4. Many-Body Methods

In the present work, we used the interacting shell model (ISM) [41] and the proton–neutron quasiparticle random-phase approximation (pnQRPA) [42] to compute the ground state wave function of ^{136}Ba and the ground and excited states of ^{136}Cs. There have been several earlier ISM calculations of the DBD characteristics of the ^{136}Xe–^{136}Cs–^{136}Ba triplet of nuclei [6–9]. In these calculations, the jj55pn model space with the single-particle orbitals $2s_{1/2}$, $1d_{3/2}$, $1d_{5/2}$, $0g_{7/2}$, and $0h_{11/2}$ was adopted for both protons and neutrons. Here, we adopted the same model space and used the sn100pn [43] interaction, whose Hamiltonian consists of neutron–neutron (nn), proton–neutron (pn), and proton–proton (pp) interactions, with the latter containing the Coulomb interaction. The single-particle energies were -9.68, -8.72, -7.34, -7.24, and -6.88 MeV for the proton and -9.74, -8.97, -7.62, -7.31, and -7.38 MeV for the neutron $0g_{7/2}$, $1d_{5/2}$, $2s_{1/2}$, $1d_{3/2}$, and $0h_{11/2}$ orbitals, respectively [43]. In Reference [8], a quenching factor $q = 0.45$ was used for the spin–isospin operator $\sigma\tau$, and in References [6,7,9], $q = 0.74$ was used. The latter quenching corresponds to a value $g_{\mathrm{A}}^{\mathrm{eff}} = 0.93$ of the effective value of the axial vector coupling. We adopted this value of $g_{\mathrm{A}}^{\mathrm{eff}}$ in this work, as benchmarked by the three mentioned ISM calculations and preferred by the quenching through the 2BC, the associated $g_{\mathrm{A}}^{\mathrm{eff}}$ interval discussed at the end of Section 2.3. In the actual ISM computations, we used the NuShellX@MSU code with its interaction libraries [44].

The pnQRPA correctly accounts for the gross features of spin–isospin strength functions, such as (p,n) and (n,p) reactions [4]. On the other hand, the pnQRPA typically poorly describes the fine structure of the low-lying states in odd–odd nuclei. In the present study, we wanted to test the capabilities of pnQRPA in producing the low-energy excitation spectrum in ^{136}Cs through the comparison of its results with those of the ISM. We used the same large, no-core, single-particle bases for protons and neutrons as in Reference [45]. These bases are based on Coulomb-corrected Woods–Saxon potential [46] and are slightly modified in the vicinity of the respective Fermi surfaces. All of the basic features of the pnQRPA are covered in detail in Reference [42]. It suffices to know that the pnQRPA is based on the BCS theory of superconductivity [47] and that the pairing strengths for the protons and neutrons were obtained through matching with the observed proton and neutron separation energies in the reference even–even nucleus [42], in this case ^{136}Ba. Furthermore, we used the method of Reference [48] to divide the renormalization of the effective two-body Bonn-A G-matrix interaction [49] into particle–hole and particle–particle parts by using the effective adjustable strength parameters g_{ph} and g_{pp}, known as the particle–hole and particle–particle strength parameters, respectively. The particle–hole parameter—g_{ph}—is typically adjusted to the centroid energy of the Gamow–Teller giant resonance (GTGR) in the adjacent odd–odd nucleus of the even–even reference nucleus. Here, we resorted to the same method and adjusted it to the known GTGR energy in ^{136}Cs [45] in order to obtain the value $g_{\mathrm{ph}} = 1.18$.

In Reference [45], a refined method concerning the g_{pp} parameter was adopted: following the original idea put forth in Reference [50], a scheme called partial isospin restoration (PIR) was adopted. In the present work, we followed the PIR by multiplying the isoscalar ($T = 0$) and isovector ($T = 1$) parts of the particle–particle matrix elements of the G-matrix by the strength parameters $g_{\mathrm{pp}}^{T=0}$ and $g_{\mathrm{pp}}^{T=1}$, respectively. The isovector strength was adjusted such that the Fermi part of the two-neutrino double-beta-decay (TNDBD) NME, corresponding to the transition $^{136}\mathrm{Xe} \rightarrow {}^{136}\mathrm{Ba}$, vanished, leading to a partial isospin restoration of the $T = 1$ proton–neutron, proton–proton, and neutron–neutron pairing channels. The isoscalar strength was subsequently varied so as to reproduce the measured half-life of the mentioned TNDBD transition [51].

3. Results and Discussion

First, we performed benchmark calculations in both the ISM and pnQRPA, omitting the 2BC contributions and using the free-nucleon value $g_{\mathrm{A}} = 1.27$ and the corresponding pseudoscalar coupling $g_{\mathrm{P}} = 8.64$ following from the Goldberger–Treiman relation (9). In the

pnQRPA calculations, we adjusted the particle–particle parameters via the PIR scheme. We will use the shorthand notations sm-1BC and qrpa-1BC for these methods henceforth. Next, we performed more realistic calculations, taking into account the missing 2BC and the deficiencies of the many-body methods. We performed four different evaluations of the OMC rates, naming them as:

sm-2BC: We performed an ISM calculation using the sn100pn interaction [43] by quenching the free axial vector couplings $g_{\rm A} = 1.27$ and $g_{\rm P} = 8.64$ using the 2BC according to Equations (10) and (11).

sm-phen: We performed an ISM calculation like above, but this time, we used the phenomenologically obtained quenched value $g_{\rm A}^{\rm eff} = 0.93$ [9] and the value $g_{\rm P}^{\rm eff} = 6.32$ obtained through the Goldberger–Treiman relation (9).

qrpa-2BC: We used the pnQRPA method as described in Section 2.4 and quenched $g_{\rm A}$ and $g_{\rm P}$ with the 2BC using Equations (10) and (11). We used the PIR scheme and adjusted the isoscalar strength to a value of $g_{\rm pp}^{T=1} = 0.86$ in order to achieve the partial isospin restoration, then we adjust the isoscalar strength to the values $g_{\rm pp}^{T=0} = 0.65$ ($g_{\rm pp}^{T=0} = 0.67$) in order to reproduce the TNDBD half-life $t_{1/2}^{(2\nu)} = (2.18 \pm 0.05) \cdot 10^{21}$ yr [51] using the effective coupling $g_{\rm A}^{\rm eff} = 0.89$ ($g_{\rm A}^{\rm eff} = 1.02$) corresponding to the free nucleon value $g_{\rm A} = 1.27$ quenched by the zero-momentum transfer correction $\delta_a(0)$ through Equation (10) with parameters $\rho = 0.09$ fm^{-3} and $c_D = -6.08$ ($\rho = 0.11$ fm^{-3} and $c_D = 0.30$).

qrpa-phen: Again, we used the pnQRPA method like above, but we used as the particle–particle strength the value $g_{\rm pp}^{T=0} = g_{\rm pp}^{T=1} = 0.7$, which was obtained from the extensive survey of the β-decay and TNDBD half-lives within the mass range $A = 100$–136 in Reference [52]. We adopted the effective coupling $g_{\rm A}^{\rm eff} = 0.83$ resulting from the so-called linear $g_{\rm A}$ model of the same work. This value is somewhat below the range of values $g_{\rm A}^{\rm eff} = 0.89$–$1.02$ corresponding to the axial vector correction $\delta_a(0)$ at zero-momentum transfer. The corresponding effective pseudoscalar coupling is $g_{\rm P}^{\rm eff} = 5.64$, as obtained through the Goldberger–Treiman relation (9). The value $g_{\rm A}^{\rm eff} = 0.83$ can be considered to account for both the missing two-body currents at $q = 0$ MeV and the deficiencies of the many-body approach in the spirit of Reference [16]. However, it does not take into account the momentum dependence of the two-body currents.

A summary of the values of all of the involved couplings and parameters is made in Table 1. We only considered the OMC rates of states with angular momenta $J \leq 5$, since the OMC rates of states with higher angular momenta are negligible.

Table 1. Values of the weak axial couplings, the Fermi gas density ρ, and the LEC c_D and pnQRPA parameters used in our calculations.

	sm-1BC and sm-2BC		**sm-phen**	**qrpa-1BC**	**qrpa-2BC**		**qrpa-phen**
$g_{\rm PP}^{\rm T=0}$	-		-	0.69	0.65	0.67	0.7
$g_{\rm PP}^{\rm T=1}$	-		-	0.86	0.86	0.86	0.7
$g_{\rm ph}$	-		-	1.18	1.18	1.18	1.18
g_A	1.27		0.93	1.27	1.27	1.27	0.83
g_P/g_A	6.8		6.8	6.8	6.8	6.8	6.8
ρ	0.09	0.11	-	-	0.09	0.11	-
c_D	-6.08	0.30	-	-	-6.08	0.30	-

We started by comparing the calculated ISM and pnQRPA excitation spectra of ^{136}Cs with the experimental ones, the results being shown in Figure 3. The pnQRPA calculations were conducted according to the schemes **qrpa-2BC** and **qrpa-phen**. It is worth noting

that there are three sets of the pnQRPA-computed energies based on the three different values of the ($g_{pp}^{T=0}$, $g_{pp}^{T=1}$) pairs used in the pnQRPA calculations. Here, we plotted just one set of energies in the **qrpa-2BC** scheme, since the two sets of energy are almost identical. From Figure 3, it can be seen that the densities of both the ISM- and pnQRPA-computed states are quite similar, higher than the densities of the measured states. It is, in fact, remarkable that both theories predict low-energy spectra so similarly, with pnQRPA able to reproduce the density of the ISM states. The density of the experimental spectrum is smaller than predicted by the computations, probably due to difficulties in observing some of the states.

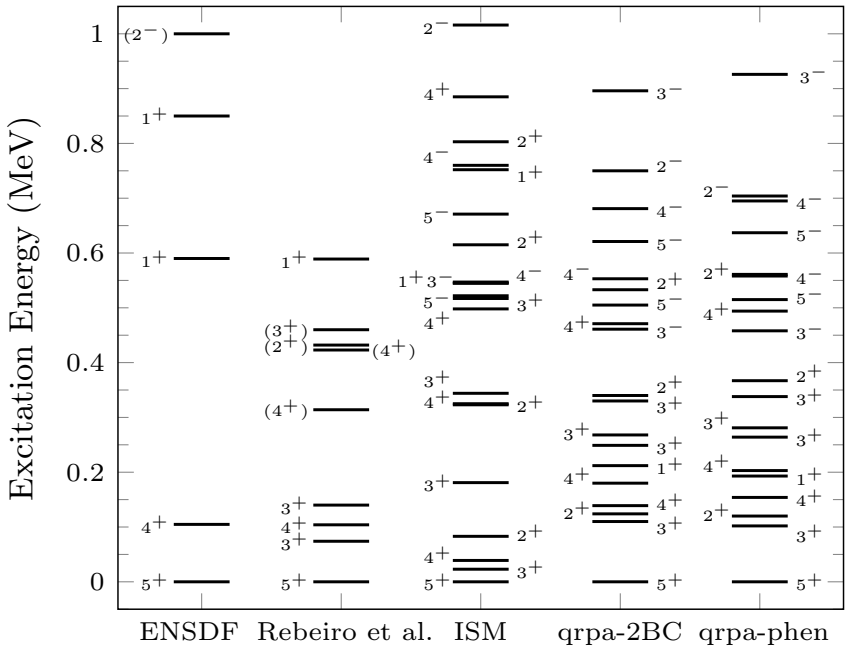

Figure 3. Excitation energy spectrum of ^{136}Cs. A comparison between the experimental spectrum and those computed by using the ISM and pnQRPA is shown here. The first experimental spectrum was taken from the ENSDF database [53], and the second one was taken from Rebeiro et al. in Reference [54]. Only states with angular momenta $J \leq 5$ were considered.

The results of the OMC calculations are presented in Table 2 (ISM results) and Table 3 (pnQRPA results). In Table 2, the first column displays the spin parity of the final state and the second column its excitation energy in MeV (in order of increasing energy). The third to fifth columns give the ISM-computed OMC rates in units of 10^3 1/s. The third column (1BC) corresponds to an ISM calculation without the 2BC contribution, and the fourth column corresponds to the same calculation with the 2BC contribution included (the **sm-2BC** calculational scheme). The fifth column lists the OMC rates obtained by using the phenomenological **sm-phen** calculational scheme. Table 3 has a similar structure, but now there are two sets of **qrpa-2BC** energies (column 2) corresponding to the two sets of LEC used in our calculations and the set of **qrpa-phen** energies in column 3. Columns 4–6 list the OMC rates obtained by using the schemes **qrpa-1BC**, **qrpa-2BC**, and **qrpa-phen**.

The first observation from columns three and four of Tables 2 and 3 is that the two-body currents, included either via the 2BC corrections $\delta_a(q^2)$ and $\delta_a^P(q^2)$ or phenomenologically via effective couplings, affect the OMC rates considerably, on average by some (30–40)%, but up to almost 50% in some cases.

Table 2. ISM-computed energies (second column) and OMC rates (third to fifth columns) of the final states (f) of spin J and parity π (first column) with angular momenta $J \leq 5$. The bottom line summarizes the total OMC rates below some 1 MeV as summed over the OMC rates listed in columns three to five. The lower (upper) limits in column four correspond to the Fermi gas density $\rho = 0.09$ fm^{-3} and the low-energy constant $c_D = -6.08$ ($\rho = 0.11$ fm^{-3} and $c_D = 0.3$), the rest of the LEC being equal in the two sets.

		OMC Rate (10^3 1/s)		
J_f^π	**E(MeV)**	**sm-1BC**	**sm-2BC**	**sm-phen**
5_1^+	0.000	0.0647	0.0661 (0.0836)	0.0433
3_1^+	0.023	4.02	2.75 (3.36)	2.60
4_1^+	0.039	1.50	1.36 (1.40)	1.37
2_1^+	0.083	10.6	5.62 (6.99)	6.18
3_2^+	0.181	12.0	6.24 (8.08)	6.66
2_2^+	0.225	20.1	12.8 (15.00)	13.7
3_3^+	0.244	4.94	2.48 (3.23)	2.71
4_2^+	0.323	5.83	3.50 (4.17)	3.78
4_3^+	0.498	6.00	4.34 (4.83)	4.54
3_4^+	0.517	31.2	16.8 (21.5)	17.9
5_1^-	0.522	0.645	0.371 (0.451)	0.404
3_1^-	0.545	16.1	8.85 (11.0)	9.73
1_1^+	0.545	9.01	4.67 (6.03)	5.03
4_1^-	0.547	24.0	13.0 (16.7)	13.7
2_3^+	0.615	18.2	12.5 (14.2)	13.2
5_2^-	0.671	0.251	0.190 (0.208)	0.198
1_2^+	0.752	0.285	0.123 (0.163)	0.146
4_2^-	0.760	2.22	1.31 (1.65)	1.32
2_4^+	0.803	2.49	1.74 (1.95)	1.83
4_4^+	0.885	0.143	0.0865 (0.103)	0.0933
2_1^-	1.016	78.6	41.5 (53.3)	44.4
Sum (10^3 1/s)		248	140 (174)	150

The total rates of these states are summarized in Table 4, indicating that in both models, the most important contributions come from the 1^+, 2^+, 2^-, and 3^+ states. The pnQRPA states are able to catch more collectivity of the 1^+ and 2^+ states, particularly for the 1_1^+ state, which is quite collective in the pnQRPA.

In order to relate the pnQRPA results to previous measurements, one can take a look at the computations in Reference [37]. There, the rates of the OMC of several double-beta daughter nuclei, particularly of ^{136}Ba, were computed by using large, no-core, single-particle spaces and the effective Bonn-A potential, quite like in the present work. In those calculations, the effective values $g_{\rm A}^{\rm eff} = 0.80$ and $g_{\rm P}^{\rm eff} = 7.0$ were adopted, which are values close to those of our **qrpa-phen** scheme and not far from our **qrpa-2BC** calculational scheme. This makes the three computations very comparable, particularly for the OMC of ^{136}Ba, but also for ^{76}Se, where experimental data exist. In Table V of Reference [37], the pnQRPA-computed OMC rates of final states in ^{76}As, below some 1 MeV of excitation like in the present work, were compared with the corresponding experimental ones, and a surprisingly good correspondence was found. There, the total rate for the OMC of the 0^+, 1^+, 1^-, 2^+, 2^-, 3^+, 3^-, 4^+, and 4^- final states in ^{76}As was 665×10^3 1/s in the experiment and 675×10^3 1/s in the pnQRPA. These total OMC rates are in line with the total OMC rates of (674–807) $\times 10^3$ 1/s and 592×10^3 1/s of our **qrpa-2BC** and **qrpa-phen** calculational schemes, respectively. Notably, both in the experiment and in the pnQRPA calculation

of Reference [37], the 1^+ rate was the largest one with the values 218×10^3 1/s for the experiment and 237×10^3 1/s for the pnQRPA, comparable with our (243–303) $\times 10^3$ 1/s and 207×10^3 1/s in the **qrpa-2BC** and **qrpa-phen** calculational schemes. In Reference [37] also, the OMC of 2^- states was strong, some 10 times stronger than in the present calculations, since the role of 2^- states in pf-shell nuclei is quite pronounced [4].

Table 3. pnQRPA-computed energies for the **qrpa-2BC** scheme (second column) and the **qrpa-phen** scheme (third column) and OMC rates (fourth to sixth columns) of the final states (f) of spin J and parity π (first column) with angular momenta $J \leq 5$. The bottom line summarizes the total OMC rates below 1 MeV as summed over the OMC rates listed in columns four to six. The two energies in column two and the lower (upper) limits in column five correspond to the Fermi gas density $\rho = 0.09$ fm^{-3} and the low-energy constant $c_D = -6.08$ ($\rho = 0.11$ fm^{-3} and $c_D = 0.3$), the rest of the LEC being equal in the two sets.

			OMC Rate (10^3 1/s)		
J_f^π	E(MeV) qrpa-2BC	E(MeV) qrpa-phen	qrpa-1BC	qrpa-2BC	qrpa-phen
5_1^+	0.000	0.000	0.902	0.491 (0.601)	0.483
3_1^+	0.110 (0.107)	0.102	3.04	1.74 (2.19)	1.51
2_1^+	0.124 (0.122)	0.120	133	102 (111)	93.3
4_1^+	0.139 (0.144)	0.154	10.0	8.81 (9.34)	8.96
1_1^+	0.227 (0.213)	0.193	443	243.0 (303.4)	206.9
4_2^+	0.180 (0.179)	0.203	12.4	8.76 (9.61)	8.25
3_2^+	0.249 (0.254)	0.264	11.6	7.93 (10.8)	3.49
3_3^+	0.268 (0.273)	0.281	156	85.6 (108)	77.5
3_4^+	0.330 (0.332)	0.338	12.2	9.50 (11.9)	5.34
2_2^+	0.340 (0.346)	0.367	88.3	49.0 (60.2)	50.1
3_1^-	0.461 (0.459)	0.458	48.0	28.9 (34.4)	25.8
4_3^+	0.471 (0.477)	0.494	4.19	3.24 (3.60)	3.18
5_1^-	0.505 (0.509)	0.515	1.20	0.825 (0.933)	0.775
4_1^-	0.553 (0.555)	0.558	1.60	1.04 (1.19)	0.596
2_3^+	0.533 (0.538)	0.561	87.1	60.0 (68.3)	57.7
5_2^-	0.621 (0.624)	0.637	0.017	0.0135 (0.0149)	0.0178
4_2^-	0.681 (0.686)	0.695	43.1	24.1 (30.6)	20.5
2_1^-	0.750 (0.725)	0.704	27.3	26.6 (26.0)	14.2
3_2^-	0.896 (0.901)	0.926	20.5	12.7 (15.1)	12.9
Sum (10^3 1/s)			1103	674 (807)	592

The measured total rate in ^{136}Ba, including all of the possible final states, features 11,100 $\times 10^3$ 1/s [55]. This means that the OMC rate of states below 1 MeV accounts for some 1.5% of the total rate for the **sm-2BC** scheme, 1.4% of the total rate for the **sm-phen** scheme, 6–7% of the total rate for the **qrpa-2BC** scheme, and 5.3% of the total rate for the **qrpa-phen** scheme, thus being below 10% but still non-negligible. This highlights the importance of comparison with the potential future experimental data and the emerging implications for the virtual NDBD transitions below roughly 1 MeV of excitation in the intermediate nucleus of a double-beta triplet of nuclei.

In the end, it would be highly interesting to compare the presently computed OMC rates to individual final states and the total OMC rate below 1 MeV with future experimental results by the MONUMENT Collaboration [56]. This will open up the possibility to probe the nuclear wave functions within the considered 1 MeV excitation energy interval in ^{136}Cs. At the same time, we can gain information on the value of both $g_{\rm A}$ and $g_{\rm P}$, the weak axial coupling and the induced pseudoscalar coupling, in a momentum-exchange range

relevant for the NDBD [22]. This gained information helps improve the precision of the nuclear matrix elements of the NDBD and thus reflects on the sensibility estimates of presently-running and future NDBD experiments.

Table 4. Total OMC rates of each multipole J^π as summed over the rates listed in Table 2 for the **sm-2BC** and **sm-phen** schemes and in Table 3 for the **qrpa-2BC** and **qrpa-phen** schemes. The lower (upper) limits in the second and fourth columns correspond to the Fermi gas density $\rho = 0.09$ fm^{-3} and the low-energy constant $c_D = -6.08$ ($\rho = 0.11$ fm^{-3} and $c_D = 0.3$).

	OMC Rate (10^3 1/s)			
J^π	**sm-2BC**	**sm-phen**	**qrpa-2BC**	**qrpa-phen**
5^+	0.1 (0.1)	0.0	0.5 (0.6)	0.5
4^+	9.3 (10.5)	9.8	20.8 (22.6)	20.4
3^+	28.3 (36.2)	29.9	104.8 (132.9)	87.8
2^+	32.7 (38.1)	34.9	211.0 (239.5)	201.1
1^+	4.8 (6.2)	5.2	243.0 (303.4)	206.9
5^-	0.6 (0.7)	0.6	0.8 (0.9)	0.8
4^-	14.3 (18.4)	15.0	25.1 (31.8)	21.2
3^-	8.9 (11.0)	9.7	41.6 (49.5)	38.7
2^-	41.5 (53.3)	44.4	26.6 (26.0)	14.2

4. Conclusions

In the present work, we computed the rates of ordinary muon capture on ^{136}Ba to low-lying nuclear states (below roughly 1 MeV of excitation energy) in ^{136}Cs, ^{136}Ba being the daughter nucleus of ^{136}Xe double-beta decay. The capture rates were computed by using the interacting shell model (ISM) and proton–neutron quasiparticle random-phase approximation (pnQRPA). Furthermore, the chiral two-body meson-exchange currents and the exact *s*-orbital Dirac wave function of the captured muon were used in the numerical computations. The computed energy spectra and the capture rates below 1 MeV of excitation in ^{136}Cs were surprisingly similar for both the ISM and the pnQRPA, the experimental low-energy spectrum being less dense. The chiral two-body currents reduce the capture rates by some (30–40)% on average, and the summed capture rates below 1 MeV of excitation in ^{136}Cs account for some (1–7)% of the total measured capture rate, thus being potentially a sizable portion of the total capture rate. Comparison of the capture rates with future experimental data opens up possibilities for accessing the wave functions of low-energy states in ^{136}Cs and the effective values of the weak axial-type couplings, relevant for the neutrinoless double-beta decay of ^{136}Xe and beyond.

Author Contributions: Ordinary muon capture rates and pnQRPA calculations, P.G.; parameter values and supervision of the computations, L.J.; calculation of the relativistic muon wave function, J.K.; nuclear shell-model calculations, M.R.; original idea of the project, coordination and supervision of the computations, and writing of the first draft of the paper, J.S. All authors have read and agreed to the published version of the manuscript.

Funding: This research was funded by the Academy of Finland, grants No. 314733, No. 320062, and No. 345869 and by the Arthur B. McDonald Canadian Astroparticle Physics Research Institute. TRIUMF received federal funding via a contribution agreement with the National Research Council of Canada.

Data Availability Statement: Not applicable.

Conflicts of Interest: The authors declare no conflicts of interest.

Note

[1] In the present work, we use the convention $c = 1$ for compactness of presentation.

References

1. Suhonen, J.; Civitarese, O. Weak-interaction and nuclear-structure aspects of nuclear double beta decay. *Phys. Rep.* **1998**, *300*, 123–214. [CrossRef]
2. Vergados, J.D.; Ejiri, H.; Šimkovic, F. Neutrinoless double beta decay and neutrino mass. *Int. J. Mod. Phys. E* **2016**, *25*, 1630007. [CrossRef]
3. Engel, J.; Menéndez, J. Status and future of nuclear matrix elements for neutrinoless double-beta decay: A review. *Rep. Prog. Phys.* **2017**, *80*, 046301. [CrossRef] [PubMed]
4. Ejiri, H.; Suhonen, J.; Zuber, K. Neutrino-nuclear responses for astro-neutrinos, single beta decays and double beta decays. *Phys. Rep.* **2019**, *797*, 1–102. [CrossRef]
5. Agostini, M.; Benato, G.; Detwiler, J.A.; Menéndez, J.; Vissani, F. Toward the discovery of matter creation with neutrinoless double-beta decay. *arXiv* **2022**, arXiv:2202.01787.
6. Caurier, E.; Nowacki, F.; Poves, A.; Retamosa, J. Shell Model Studies of the Double Beta Decays of ^{76}Ge, ^{82}Se, and ^{136}Xe. *Phys. Rev. Lett.* **1996**, *77*, 1954–1957. [CrossRef]
7. Caurier, E.; Menéndez, J.; Nowacki, F.; Poves, A. Influence of Pairing on the Nuclear Matrix Elements of the Neutrinoless $\beta\beta$ Decays. *Phys. Rev. Lett.* **2008**, *100*, 052503. [CrossRef]
8. Caurier, E.; Nowacki, F.; Poves, A. Shell Model description of the $\beta\beta$ decay of 136Xe. *Phys. Lett. B* **2012**, *711*, 62–64. . [CrossRef]
9. Horoi, M.; Brown, B.A. Shell-Model Analysis of the ^{136}Xe Double Beta Decay Nuclear Matrix Elements. *Phys. Rev. Lett.* **2013**, *110*, 222502. [CrossRef]
10. Suhonen, J.; Civitarese, O. Double-beta-decay nuclear matrix elements in the QRPA framework. *J. Phys. G Nucl. Part. Phys.* **2012**, *39*, 085105. [CrossRef]
11. Märkisch, B.; Mest, H.; Saul, H.; Wang, X.; Abele, H.; Dubbers, D.; Klopf, M.; Petoukhov, A.; Roick, C.; Soldner, T.; et al. Measurement of the Weak Axial-Vector Coupling Constant in the Decay of Free Neutrons Using a Pulsed Cold Neutron Beam. *Phys. Rev. Lett.* **2019**, *122*, 242501. [CrossRef]
12. Suhonen, J.T. Value of the Axial-Vector Coupling Strength in β and $\beta\beta$ Decays: A Review. *Front. Phys.* **2017**, *5*, 55. [CrossRef]
13. Ejiri, H. Axial-vector weak coupling at medium momentum for astro neutrinos and double beta decays. *J. Phys. G Nucl. Part. Phys.* **2019**, *46*, 125202. [CrossRef]
14. Ejiri, H. Nuclear Matrix Elements for β and $\beta\beta$ Decays and Quenching of the Weak Coupling $g_{\rm A}$ in QRPA. *Front. Phys.* **2019**, *7*, 30. [CrossRef]
15. Menéndez, J.; Gazit, D.; Schwenk, A. Chiral Two-Body Currents in Nuclei: Gamow-Teller Transitions and Neutrinoless Double-Beta Decay. *Phys. Rev. Lett.* **2011**, *107*, 062501. [CrossRef] [PubMed]
16. Gysbers, P.; Hagen, G.; Holt, J.; Jansen, G.; Morris, T.; Navrátil, P.; Papenbrock, T.; Quaglioni, S.; Schwenk, A.; Stroberg, S.; et al. Discrepancy between experimental and theoretical β-decay rates resolved from first principles. *Nat. Phys.* **2019**, *15*, 1. [CrossRef]
17. Morita, M.; Fujii, A. Theory of Allowed and Forbidden Transitions in Muon Capture Reactions. *Phys. Rev.* **1960**, *118*, 606–618. [CrossRef]
18. Jokiniemi, L.; Miyagi, T.; Stroberg, S.R.; Holt, J.D.; Kotila, J.; Suhonen, J. Ab initio calculation of muon capture on ^{24}Mg. *Phys. Rev. C* **2023**, *107*, 014327. [CrossRef]
19. Measday, D. The nuclear physics of muon capture. *Phys. Rep.* **2001**, *354*, 243–409. . [CrossRef]
20. Kortelainen, M.; Suhonen, J. Ordinary muon capture as a probe of virtual transitions of $\beta\beta$ decay. *Europhys. Lett.* **2002**, *58*, 666. [CrossRef]
21. Kortelainen, M.; Suhonen, J. Nuclear muon capture as a powerful probe of double-beta decays in light nuclei. *J. Phys. G Nucl. Part. Phys.* **2004**, *30*, 2003. [CrossRef]
22. Siiskonen, T.; Hjorth-Jensen, M.; Suhonen, J. Renormalization of the weak hadronic current in the nuclear medium. *Phys. Rev. C* **2001**, *63*, 055501. [CrossRef]
23. Jokiniemi, L.; Suhonen, J. Comparative analysis of muon-capture and $0\nu\beta\beta$-decay matrix elements. *Phys. Rev. C* **2020**, *102*, 024303. [CrossRef]
24. Asakura, K.; Gando, A.; Gando, Y.; Hachiya, T.; Hayashida, S.; Ikeda, H.; Inoue, K.; Ishidoshiro, K.; Ishikawa, T.; Ishio, S.; et al. Search for double-beta decay of ^{136}Xe to excited states of ^{136}Ba with the KamLAND-Zen experiment. *Nucl. Phys. A* **2016**, *946*, 171–181. [CrossRef]
25. Albert, J.B.; Anton, G.; Badhrees, I.; Barbeau, P.S.; Bayerlein, R.; Beck, D.; Belov, V.; Breidenbach, M.; Brunner, T.; Cao, G.F.; et al. Search for Neutrinoless Double-Beta Decay with the Upgraded EXO-200 Detector. *Phys. Rev. Lett.* **2018**, *120*, 072701. [CrossRef]
26. Shimizu, I.; Chen, M. Double Beta Decay Experiments With Loaded Liquid Scintillator. *Front. Phys.* **2019**, *7*, 33. [CrossRef]
27. Kharusi, S.; Anton, G.; Badhrees, I.; Barbeau, P.; Beck, D.; Belov, V.; Bhatta, T.; Breidenbach, M.; Brunner, T.; Cao, G.; et al. Search for Majoron-emitting modes of Xe 136 double beta decay with the complete EXO-200 dataset. *Phys. Rev. D* **2021**, *104*, 112002. [CrossRef]
28. The MONUMENT Collaboration, see the Contribution List of the MEDEX'22 Workshop, Prague, Czech Republic, 13–17 June 2022. Available online: https://indico.utef.cvut.cz/event/32/contributions (accessed on 3 June 2023) .
29. Measday, D.F.; Stocki, T.J.; Ricardo, A.; Cole, P.L.; Chaden, D.; Fernando, U. Comparison of Muon Capture in Light and in Heavy Nuclei. *AIP Conf. Proc.* **2007**, *947*, 253. [CrossRef]
30. Measday, D.F.; Stocki, T.J.; Tam, H. Gamma rays from muon capture in I, Au, and Bi. *Phys. Rev. C* **2007**, *75*, 045501. [CrossRef]

31. Hashim, I.H.; Ejiri, H.; Shima, T.; Takahisa, K.; Sato, A.; Kuno, Y.; Ninomiya, K.; Kawamura, N.; Miyake, Y. Muon capture reaction on ^{100}Mo to study the nuclear response for double-β decay and neutrinos of astrophysics origin. *Phys. Rev. C* **2018**, *97*, 014617. [CrossRef]
32. Hashim, I.H.; Ejiri, H. New Research Project with Muon Beams for Neutrino Nuclear Responses and Nuclear Isotopes Production. *AAPPS Bull.* **2019**, *29*, 21–26. [CrossRef]
33. Hashim, I.; Ejiri, H.; Othman, F.; Ibrahim, F.; Soberi, F.; Ghani, N.; Shima, T.; Sato, A.; Ninomiya, K. Nuclear isotope production by ordinary muon capture reaction. *Nucl. Instrum. Methods Phys. Res. Sect. A Accel. Spectrometers Detect. Assoc. Equip.* **2020**, *963*, 163749. [CrossRef]
34. Hashim, I.H.; Ejiri, H. Ordinary Muon Capture for Double Beta Decay and Anti-Neutrino Nuclear Responses. *Front. Astron. Space Sci.* **2021**, *8*, 666383. [CrossRef]
35. Bethe, H.; Salpeter, E. *Quantum Mechanics of One- and Two-Electron Atoms*; Academic Press: New York, NY, USA, 1959.
36. Jokiniemi, L.; Suhonen, J.; Ejiri, H.; Hashim, I. Pinning down the strength function for ordinary muon capture on 100Mo. *Phys. Lett. B* **2019**, *794*, 143–147. . [CrossRef]
37. Jokiniemi, L.; Suhonen, J. Muon-capture strength functions in intermediate nuclei of $0\nu\beta\beta$ decays. *Phys. Rev. C* **2019**, *100*, 014619. [CrossRef]
38. Hoferichter, M.; Menéndez, J.; Schwenk, A. Coherent elastic neutrino-nucleus scattering: EFT analysis and nuclear responses. *Phys. Rev. D* **2020**, *102*, 074018. [CrossRef]
39. Klos, P.; Menéndez, J.; Gazit, D.; Schwenk, A. Large-scale nuclear structure calculations for spin-dependent WIMP scattering with chiral effective field theory currents. *Phys. Rev. D* **2013**, *88*, 083516. [CrossRef]
40. Jokiniemi, L.; Romeo, B.; Soriano, P.; Menéndez, J. Neutrinoless $\beta\beta$-decay nuclear matrix elements from two-neutrino $\beta\beta$-decay data. *Phys. Rev. C* **2022**, *107*, 044305. [CrossRef]
41. Caurier, E.; Martínez-Pinedo, G.; Nowacki, F.; Poves, A.; Zuker, A.P. The shell model as a unified view of nuclear structure. *Rev. Mod. Phys.* **2005**, *77*, 427–488. [CrossRef]
42. Suhonen, J. *From Nucleons to Nucleus: Concepts of Microscopic Nuclear Theory*; Theoretical and Mathematical Physics; Springer: Berlin/Heidelberg, Germany, 2007. [CrossRef]
43. Brown, B.A.; Stone, N.J.; Stone, J.R.; Towner, I.S.; Hjorth-Jensen, M. Magnetic moments of the 2_1^+ states around ^{132}Sn. *Phys. Rev. C* **2005**, *71*, 044317. [CrossRef]
44. Brown, B.; Rae, W. The Shell-Model Code NuShellX@MSU. *Nucl. Data Sheets* **2014**, *120*, 115–118. 2014.07.022. [CrossRef]
45. Jokiniemi, L.; Ejiri, H.; Frekers, D.; Suhonen, J. Neutrinoless $\beta\beta$ nuclear matrix elements using isovector spin-dipole $J^\pi = 2^-$ data. *Phys. Rev. C* **2018**, *98*, 024608. [CrossRef]
46. Bohr, A.; Mottelson, B.R. *Nuclear Structure*; Benjamin: New York, NY, USA, 1969; Volume I.
47. Bardeen, J.; Cooper, L.N.; Schrieffer, J.R. Microscopic Theory of Superconductivity. *Phys. Rev.* **1957**, *106*, 162–164. [CrossRef]
48. Suhonen, J.; Taigel, T.; Faessler, A. pnQRPA calculation of the β^+/EC quenching for several neutron-deficient nuclei in mass regions A = 94–110 and A =146–156. *Nucl. Phys. A* **1988**, *486*, 91–117. [CrossRef]
49. Holinde, K. Two-nucleon forces and nuclear matter. *Phys. Rep.* **1981**, *68*, 121–188. [CrossRef]
50. Šimkovic, F.; Rodin, V.; Faessler, A.; Vogel, P. $0\nu\beta\beta$ and $2\nu\beta\beta$ nuclear matrix elements, quasiparticle random-phase approximation, and isospin symmetry restoration. *Phys. Rev. C* **2013**, *87*, 045501. [CrossRef]
51. Barabash, A. Precise Half-Life Values for Two-Neutrino Double-β Decay: 2020 review. *Universe* **2020**, *6*, 159. [CrossRef]
52. Pirinen, P.; Suhonen, J. Systematic approach to β and $2\nu\beta\beta$ decays of mass $A = 100$–136 nuclei. *Phys. Rev. C* **2015**, *91*, 054309. [CrossRef]
53. ENSDF Database. Available online: http://www.nndc.bnl.gov/ensdf/ (accessed on 3 June 2023).
54. Rebeiro, B.M.; Triambak, S.; Garrett, P.E.; Ball, G.C.; Brown, B.A.; Menéndez, J.; Romeo, B.; Adsley, P.; Lenardo, B.G; Lindsay, R.; et al. $^{138}Ba(d,\alpha)$ Study of States in ^{136}Cs: Implications for New Physics Searches with Xenon Detectors. *arXiv* **2023**, arXiv:2301.11371.
55. Suzuki, T.; Measday, D.F.; Roalsvig, J.P. Total nuclear capture rates for negative muons. *Phys. Rev. C* **1987**, *35*, 2212–2224. [CrossRef]
56. The MONUMENT Collaboration. Work in progress.